GDCh Research Article Angewandte International Edition Chemie www.angewandte.org

How to cite: *Angew. Chem. Int. Ed.* **2024**, *63*, e202412964
doi.org/10.1002/anie.202412964

CO_2 Photoreduction

Precisely Regulating Asymmetric Charge Distribution by Single-Atom Central Doped Ag-Based Series Clusters for Enhanced Photoreduction of CO_2 to Alcohol Fuels

Liu Huang, Rui Lu, Wenchang Zhang, Yikang Fan, Yuanxin Du, Kun Ni,* Yanwu Zhu, and Manzhou Zhu**

Abstract: High efficiently photocatalytic CO_2 reduction (CO_2RR) into liquid fuels in pure water system remains challenged. Iron polyphthalocyanine (FePPc) with strong light harvesting, unique Fe-N_4 structure, abundant pores, and good stability could serve as a promising catalyst for CO_2 photoreduction. To further improve the catalytic efficiency, herein, symmetry-breaking Fe sites are constructed by coupling with atomically precise M_1Ag_{24} (M=Ag, Au, Pt) series clusters. Especially, the introduction of Pt_1Ag_{24} causes the most asymmetric charge distribution of Fe in FePPc (followed by Au_1Ag_{24} and Ag_{25}), leading to the favorable CO_2 adsorption and activation. In addition, Pt_1Ag_{24}-FePPc exhibits the most effective photogenerated carriers transfer and separation. As a result, Pt_1Ag_{24}-FePPc shows the methanol/ethanol yield of 48.55/32.97 $\mu mol \cdot g_{cat}^{-1} \cdot h^{-1}$ in H_2O-CO_2 system under visible light irradiation, ~1.65/1.25-fold, 1.83/1.37-fold, and 3.60/1.61-fold higher than that of Au_1Ag_{24}-FePPc, Ag_{25}-FePPc, and FePPc, respectively. This work provides a concept for precisely construction and regulation symmetry-breaking sites of cluster-based catalysts for effective CO_2 conversion.

Introduction

With the acceleration of industrialization, the emission of CO_2 has greatly increased, resulting in serious environmental problems and energy crises. Photocatalytic CO_2 reduction (CO_2RR) to value-added chemicals or fuels has been considered as a sustainable and promising approach to simultaneously realize CO_2 emission reduction and resource utilization.[1] Although great efforts have been devoted in this field, most of the current researches stay on the stage of converting CO_2 to gaseous C1 products (i.e. CO, CH_4).[2] More desirable high-value liquid fuels (such as CH_3OH and C_2H_5OH) are difficult to obtain due to the complex process and sluggish kinetics of the multi-electron transfer.[3] In addition, to improve the efficiency of photocatalytic CO_2RR, organic solvents are usually used to promote CO_2 solubility and availability, and sacrificial agents are added to scavenge photogenerated hole and thus inhibit e^--h^+ recombination.[4] However, overuse of chemical agents adds extra product separation steps, production costs, and environmental risks. Therefore, achieving high efficiency photocatalytic CO_2RR to liquid fuels in pure water system is a challenging and meaningful task.

The prerequisite as well as the key for photocatalytic conversion of CO_2 is the light-utilization and the effective adsorption and activation of CO_2. Metal phthalocyanine (MPc) with unique light response property has been widely used in photocatalysis.[5] However, in most of current works, MPc exists in the form of small molecules with poor stability and tends to agglomerate during the reaction, thus impeding light absorption and reducing the catalytic activity.[6] Polymerization of MPc molecule can form 2D porous metal polyphthalocyanine (MPPc) framework material, which provides enhanced physical and chemical robustness, more exposed active sites and improved charge transfer ability.[7] Besides, the abundant pores and large specific surface area are beneficial for CO_2 adsorption.

With regard to CO_2 activation, one of the effective strategies is constructing symmetry-breaking sites.[8] The establishment of heterostructure can effectively modulate the electronic structure of MPPc and provide asymmetry sites, thus promoting the activation of CO_2. In recent years, atomically precise metal nanocluster (NC) has been applied in developing heterojunction catalyst to improve photocatalytic performance by increasing light-harvesting and charge carriers separation.[9] In addition, benefiting from the accuracy and tunability of NC composition and structure, it can be used to precisely control the electronic structure of the support via metal-support interaction.[10] Therefore, coupling MPPc with atomically precise metal NC is a

[*] L. Huang, R. Lu, Y. Fan, Y. Du, M. Zhu
Department of Materials Science and Engineering, Centre for Atomic Engineering of Advanced Materials, Key Laboratory of Structure and Functional Regulation of Hybrid Materials of Ministry of Education, Key Laboratory of Functional Inorganic Material Chemistry of Anhui Province, Anhui University, Hefei 230601, China
E-mail: duyuanxin@ahu.edu.cn
zmz@ahu.edu.cn

W. Zhang, K. Ni, Y. Zhu
CAS Key Laboratory of Materials for Energy Conversion, Department of Materials Science and Engineering, iChEM, University of Science and Technology of China, Hefei, Anhui, 230026 China
E-mail: nikun@ustc.edu.cn

M. Zhu
Anhui Tongyuan Environment Energy Saving Co. Ltd., Hefei, 230041, China

potential method to regulate charge distribution and create asymmetry sites for facilitating CO_2 activation.

In this work, M_1Ag_{24} NC (M=Ag, Au, Pt)-iron polyphthalocyanine heterostructure (M_1Ag_{24}-FePPc) is synthesized based on electrostatic attraction strategy with enhanced light utilization and charge transfer and separation efficiency. By introducing different single-atom central doped M_1Ag_{24} NCs, the electronic structure of FePPc is precisely regulated. Among the three NCs, Pt_1Ag_{24} NCs causes the most asymmetric charge distribution of FePPc, leading to the most effective adsorption and activation of CO_2, as confirmed by a series of experiments and calculations. Thereby, Pt_1Ag_{24}-FePPc exhibits the best photocatalytic CO_2RR performance with methanol yield of 48.55 $\mu mol \cdot g_{cat}^{-1} \cdot h^{-1}$ and ethanol yield of 32.97 $\mu mol \cdot g_{cat}^{-1} \cdot h^{-1}$ in pure water system.

Results and Discussion

The serial M_1Ag_{24} (M=Ag, Au, Pt) NC is synthesized according to our previously method,[11] and the molecular purity is confirmed by the electrospray ionization mass spectrometry (ESI-MS) and UV/Vis absorption spectrum (Figure S1). Iron polyphthalocyanine (FePPc) is prepared by one-step solid-phase method, and it shows characteristic X-ray diffraction (XRD) pattern, consistent with the previously reported FePPc (Figure S2a).[12] It displays the typical Fourier transform infrared spectrometer (FT-IR) peaks (at 1699, 1465, and 1371 cm^{-1}) of phthalocyanine frameworks, the peaks (at 1308 and 1150 cm^{-1}) of stretching vibration of C–N, and the vibration peak (at 945 cm^{-1}) of the metal-ligand bond (Fe–N) (Figure S2b).[12–13]

Pt_1Ag_{24} NC is selected as a representative to illustrate the synthesis of M_1Ag_{24}-FePPc composite (Figure 1a). The

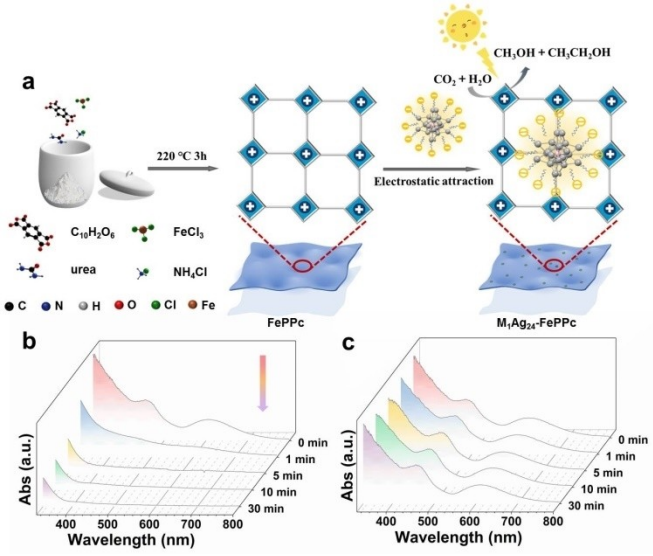

Figure 1. (a) Schematic illustration of the synthesis of M_1Ag_{24} (M = Ag, Au, Pt)-FePPc. UV − vis spectra of Pt_1Ag_{24} solution during adsorption experiments with (b) FePPc and (c) PPc.

crystal structure and the corresponding crystallographic data of Pt_1Ag_{24} are shown in Figure S3 and Table S1. Although FePPc possesses abundant pores and large specific surface area, the binding force between NC and FePPc is not simply physical adsorption, as confirmed by the control experiments with PPc (Figure 1b-c). The synthesis of Pt_1Ag_{24}-FePPc is based on electrostatic attraction strategy due to the oppositely charged feature of each other, as shown from the zeta potential results (Table S2). As shown in Figure 2a–c, Pt_1Ag_{24} NCs with an average size of 1.5 nm are uniformly dispersed on lamellar-structured FePPc. The energy dispersive X-ray spectroscopy (EDX) mapping also demonstrates the homogeneously spatial distribution of Pt, Ag, and S element on the entire FePPc substrate (Figure 2d–k). The loading amount of Pt_1Ag_{24} NC is ~3 wt % determined by inductively coupled plasma atomic emission spectrometer (ICP-AES) (Table S3). Pt_1Ag_{24}-FePPc exhibits similar XRD pattern with that of FePPc, suggesting that there is no change in crystalline structure of FePPc after introducing NC (Figure S2a). Besides, no XRD peak corresponding to metal nanoparticles is observed, also indicating that the small size of NC is maintained after combining with FePPc, in line with the transmission electron microscope (TEM) results. Pt_1Ag_{24}-FePPc not only keeps the characteristic UV/Vis absorbance peaks for B band (~300 nm) and Q band (~710 nm) of FePPc, but also shows featured signal (~455 nm) from Pt_1Ag_{24} NC.[11,14] In addition, the blue shift of Q band in Pt_1Ag_{24}-FePPc compared to FePPc indicates the strong electronic coupling between Pt_1Ag_{24} NC and FePPc (Figure S4).[14]

X-ray photoelectron spectroscopy (XPS) was used to investigate the surface chemical environments of elements in FePPc, Pt_1Ag_{24}, and Pt_1Ag_{24}-FePPc. In N 1s XPS spectrum of FePPc, the peaks at 400.65, 399.41 eV, and 398.75 eV are attributed to the Fe–N bonds, N atom linking the isoindole rings (N_β), and N atoms adjacent to the central metal atom (N_α), respectively, also confirming the M–N coordination framework structure of the FePPc (Figure S5).[12,15] For Fe 2p XPS spectrum of FePPc, the two peaks can be deconvoluted into two doublets, among which the dominating peaks at 710.65/723.72 eV are attributed to the Fe $2p_{3/2}$ and Fe $2p_{1/2}$ of Fe^{2+} and the weak signals at 713.8/728.8 eV are from corresponding orbital of Fe^{3+}, indicating the valance state of Fe is between +2 and +3.[12,15c]

After combining with Pt_1Ag_{24}, the Fe binding energy of Pt_1Ag_{24}-FePPc shows a negative shift, indicating the increase of electron density of Fe (Figure 3a). However, compared to Pt_1Ag_{24}, the binding energy of Ag for Pt_1Ag_{24}-FePPc moves to lower-region, and both Pt and S binding energy of Pt_1Ag_{24}-FePPc are shifted to higher-region, suggesting the decrease of electron density around Ag, Pt, and S (Figure 3b–d). These results also confirm the strong electronic interaction between Pt_1Ag_{24} NC and FePPc.

The XPS spectra of other NCs (Ag_{25} and Au_1Ag_{24}) before and after combining with FePPc were also performed. Compared with Ag_{25}, the binding energy of Ag and S in Ag_{25}-FePPc is decreased and increased, respectively, suggesting the decrease of electron density around Ag and S (Figure S6). For Au_1Ag_{24}, the decline in Ag binding energy

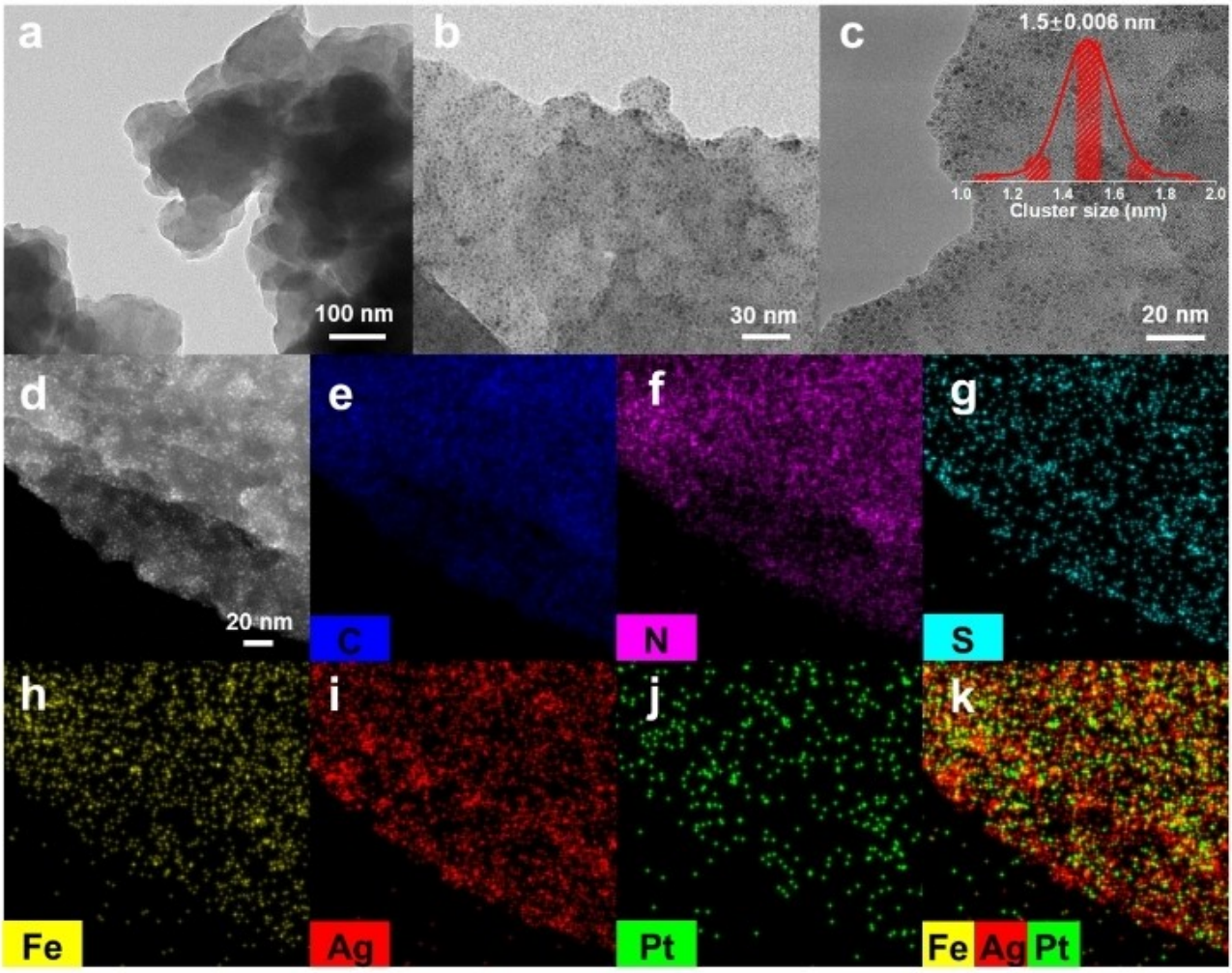

Figure 2. TEM image of (a) FePPc, (b) Pt_1Ag_{24}-FePPc, and (c) partial zoomed TEM image of Pt_1Ag_{24}-FePPc. (d–k) High-angle annular dark field scanning transmission electron microscopy (HAADF-STEM) image and corresponding EDX elemental mapping of Pt_1Ag_{24}-FePPc.

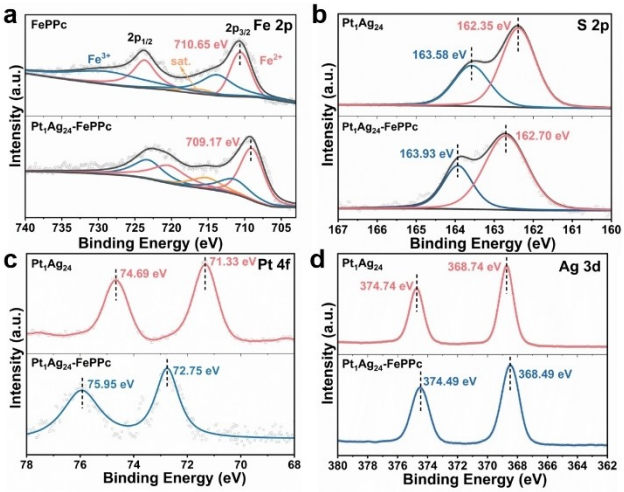

Figure 3. (a) The XPS spectra of Fe 2p for FePPc and Pt_1Ag_{24}-FePPc. The XPS spectra of (b) S 2p, (c) Pt 4f, (d) Ag 3d for Pt_1Ag_{24} and Pt_1Ag_{24}-FePPc.

and the raise in Au and S binding energy after combining with FePPc also indicate the decrease in electron density around NCs (Figure S7), which is similar to Pt_1Ag_{24} NC.

To verify the feasibility of the samples for photocatalytic CO_2RR, their energy levels were investigated. The band gap of FePPc is 1.75 eV (Figure S8a). The conduction-band (CB) and valence-band (VB) positions of FePPc are estimated to be −0.52 and 1.23 V (vs NHE, pH = 7) (Figure S8b). The Highest Occupied Molecular Orbital (HOMO) and Lowest Unoccupied Molecular Orbital (LUMO) levels of Pt_1Ag_{24} are determined as 0.41 and −1.36 V (vs NHE, pH = 7) (Figure S9). In addition, as measured from valence band XPS (VB-XPS), the VB is 1.25, 0.79, 0.69, and 0.45 eV for FePPc, Ag_{25}, Au_1Ag_{24}, and Pt_1Ag_{24}, respectively, which is basically consistent with the value measured by Tauc plots (Figure S10). Considering the reduction potential of CO_2/CH_3OH (−0.38 V) and CO_2/CH_3CH_2OH (−0.33 V) (vs NHE, pH = 7), the energy level position meets the requirements of theoretic feasibility for CO_2RR (Figure S11).[16] Other M_1Ag_{24} NCs, i.e., Ag_{25}, Au_1Ag_{24} NC were also loaded on FePPc via electrostatic attraction and applied to photo-

catalytic CO_2RR to investigate the effect of central doping on catalytic performance (Figure S4, Table S3, S4).

The photocatalytic CO_2RR was conducted in pure H_2O-CO_2 system under visible-light irradiation at 25°C room temperature by controlling with cycling condensate water. The main products are CH_3OH and CH_3CH_2OH, determined by ^1H NMR (Figure S12). Among these catalysts, Pt_1Ag_{24}-FePPc exhibits the best performance for CO_2RR with high yield rate of CH_3OH (48.55 $\mu mol \cdot g_{cat}^{-1} \cdot h^{-1}$) and CH_3CH_2OH (32.97 $\mu mol \cdot g_{cat}^{-1} \cdot h^{-1}$) (Figure 4a, S13, Table S5). Especially, the CH_3OH yield rate of Pt_1Ag_{24}-FePPc is 1.65, 1.83, and 3.60 times higher than that of Au_1Ag_{24}-FePPc (29.46 $\mu mol \cdot g_{cat}^{-1} \cdot h^{-1}$), Ag_{25}-FePPc (26.58 $\mu mol \cdot g_{cat}^{-1} \cdot h^{-1}$), and FePPc (13.48 $\mu mol \cdot g_{cat}^{-1} \cdot h^{-1}$), respectively, and the CH_3CH_2OH yield rate follows the same order. The product selectivity of the samples is shown in Figure S14. Although the yield rate of CH_3CH_2OH is lower than that of CH_3OH, the moles of effective photogenerated electrons contributed to CH_3CH_2OH production are much more than that for CH_3OH production due to the more electrons required for same amount production (Figure 4b). To best of our knowledge, the CH_3OH and CH_3CH_2OH production rates of Pt_1Ag_{24}-FePPc are in the front rank compared to the previously reported photocatalysts in pure H_2O-CO_2 system for CO_2RR (Table S6). In addition to the superior activity, Pt_1Ag_{24}-FePPc shows almost unchanged yield rate of product in consecutive five cycling tests, indicating the good stability (Figure 4c). The maintained morphology and structure after photocatalytic CO_2RR also confirms the good stability of Pt_1Ag_{24}-FePPc (Figure S15, S16).

The oxidation product yield of all the samples was carefully quantified. In CO_2-H_2O photocatalytic system, the possible H_2O oxidation product is O_2, H_2O_2, and ∫OH. Electron paramagnetic resonance (EPR) test with 5,5-dimethyl-1-pyrroline-N-oxide (DMPO) as spin-trapping reagent was conducted for •OH detection.[17] There is no •OH detected in all the samples, which is reasonable in theory because all the E_{HOMO} of M_1Ag_{24} (Ag_{25}, 0.81 V; Au_1Ag_{24}, 0.72 V; Pt_1Ag_{24}, 0.41 V) and the E_{VB} of FePPc (1.23 V) is lower than that of H_2O/•OH, 1.99 V vs NHE, pH = 7. Coloration method with N,N-dimethyl-pphenylenediamine (DPD) as indicator was conducted to detect H_2O_2.[17] Similarly, there is no H_2O_2 detected in all the samples, which is understandable because all the E_{HOMO} of M_1Ag_{24} and the E_{VB} of FePPc is lower than that of H_2O/H_2O_2, 1.37 V vs NHE, pH = 7. Online gas chromatography (GC) with a thermal conductivity detector (TCD) was used to detect the O_2 (Figure S17). None of the M_1Ag_{24} can detect O_2 due to the lower E_{HOMO} than that of H_2O/O_2, 0.82 V vs NHE, pH = 7. The E_{VB} of FePPc is higher than that of H_2O/O_2, thus FePPc and M_1Ag_{24}-FePPc can produce O_2 from the aspect of theory. The O_2 yield rate is detected to be 74.48, 98.24, 107.66, and 151.88 $\mu mol \cdot g_{cat}^{-1} \cdot h^{-1}$ for FePPc, Ag_{25}-FePPc, Au_1Ag_{24}-FePPc, and Pt_1Ag_{24}-FePPc, respectively (Figure S18), which is close to the theoretical yield based on the stoichiometric ratio (CH_3OH:O_2 = 2:3, C_2H_5OH:O_2 = 1:3), indicating the basically mass balance during the reaction.

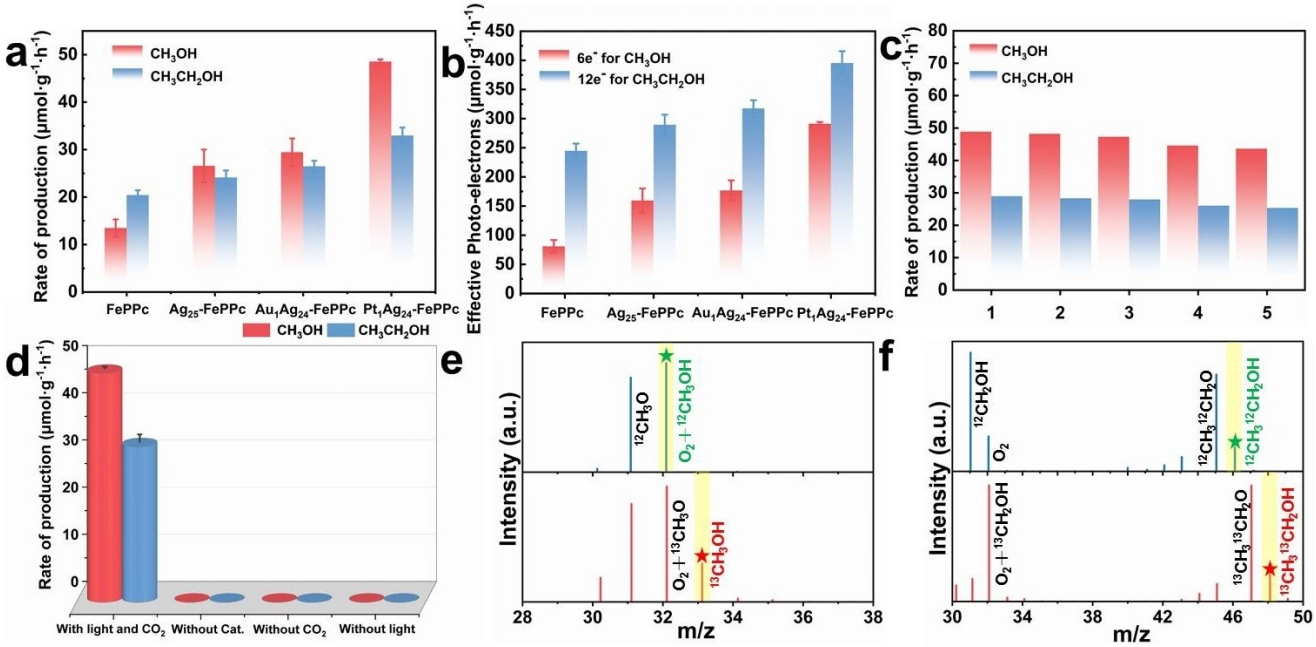

Figure 4. (a) CH_3OH and CH_3CH_2OH production rate and (b) the moles of photogenerated electrons utilized in CO_2 reduction of FePPc, Ag_{25}-FePPc, Au_1Ag_{24}-FePPc and Pt_1Ag_{24}-FePPc. (c) Recycling performance of Pt_1Ag_{24}-FePPc. (d) CH_3OH and CH_3CH_2OH production rates of Pt_1Ag_{24}-FePPc under different conditions of with light and CO_2, without catalyst, without CO_2 (Ar instead of CO_2), and without light. Error bars derived from three parallel measurements.Comparison of the mass spectra of produced (e) $^{12}CH_3OH$ and $^{13}CH_3OH$, and (f) $^{12}CH_3{}^{12}CH_2OH$ and $^{13}CH_3{}^{13}CH_2OH$ by photoreduction of $^{12}CO_2$ and $^{13}CO_2$, respectively.

A series of control experiments were conducted to confirm that the product origins from the photocatalytic CO_2RR. Under the conditions of without light, CO_2, and catalysts, the CH_3OH and CH_3CH_2OH are barely detectable (Figure 4d). $^{13}CO_2$ isotope labeling experiment were further carried out to validate that the carbon source of product. The mass peaks corresponded to $^{13}CH_3OH$, $^{13}CH_3{}^{13}CH_2OH$ and their fragments are detected when $^{13}CO_2$ is used as feed gas (Figure 4e–f, S19, S20).

The EPR test with different radical trapping agents were further conducted to invesitgate the reaction mechanism. 2,2,6,6-tetramethylpiperidinooxy (TEMPO) as the electron capture agent can be reduced to produce an EPR-silent product TEMPOH, which is usually employed to monitor the photogenerated electron.[17] As shown in Figure S21, the EPR intensity in the dark with or without catalysts is the same. After light irradiation 1 min, the EPR intensity without catalysts is almost same as that in the dark. However, after 1 min light irradiation, the EPR intensities with Pt_1Ag_{24}, FePPc, and Pt_1Ag_{24}-FePPc are all decreased, indicating the production of photogenerated electron with the three catalysts. In addition, it is worth noting that Pt_1Ag_{24}-FePPc shows the lower EPR intensity compared to pristine Pt_1Ag_{24} and FePPc, suggesting that Pt_1Ag_{24}-FePPc can effectively inhibit the recombination of photogenerated carriers and produce more available electrons, which is conducive to CO_2 reduction. DMPO (in methanol) as a spin-trapping reagent is used to verify the $^{\bullet}O_2^-$.[17] As shown in Figure S22, all the three catalysts have the signals of DMPO-$^{\bullet}O_2^-$ under light irradiation, indicating the $^{\bullet}O_2^-$ produced by the photogenerated electron injection to dissolved O_2, which satisfies the energy level position relationship (E_{LUMO} of Pt_1Ag_{24}, −1.36 V and E_{CB} of FePPc, $-0.52\ V < O_2/{}^{\bullet}O_2^-, -0.33\ V$ vs NHE, pH = 7). Besides, Pt_1Ag_{24}-FePPc shows the higher EPR signal compared to pristine Pt_1Ag_{24} and FePPc, suggesting the Pt_1Ag_{24}-FePPc can obtain more photogenerated electrons by effectively suppressing carriers recombination, which is benefit for CO_2RR. None of the samples were detected $^{\bullet}OH$, which is understandable from the energy level theory, as mentioned above. 2,2,6,6-tetramethylpiperidine (TEMP) is used to detect $^1O_2$.[17] Under light irradiation, none of the three catalysts have the $^1O_2$ signal. It is expected because in the system, the only way of producing $^1O_2$ is through two-step process (firstly, e^- reduces dissolved O_2 to produce $^{\bullet}O_2^-$, then h^+ oxidizes $^{\bullet}O_2^-$ to produced $^1O_2$), in which carriers may not survive such long time.

To further investigate the charge transfer pathway in Pt_1Ag_{24}-FePPc, in situ XPS spectra with and without light irradiation were performed. As shown in Figure S23, the binding energy of Fe is increased under light irradiation, indicating the electron density decrease of FePPc. The positive shift in Ag binding energy and the negative shift in Pt binding energy under light irradiation indicate the electron density increase of Pt_1Ag_{24}. The results show that the migration direction of the photogenerated electrons is from FePPc to Pt_1Ag_{24}, which is in line with the proposed transfer pathway. Besides, Pt_1Ag_{24}-FePPc can produce O_2, also confirming the photogenerated charge transfer direction from the aspect of energy level theory.

To explore the reason for the differences in photocatalytic CO_2RR performance of the serial M_1Ag_{24}-FePPc (M=Ag, Au, Pt), the light absorption property and photogenerated charge carriers separation efficiency were investigated. All the M_1Ag_{24}-FePPc show the enhanced light absorption compared with the FePPc (Figure S4). Pt_1Ag_{24}-FePPc exhibits the highest photocurrent response and smallest electrical resistance, indicating the effective transfer and separation of photogenerated charge carriers (Figure 5a, b). Besides, the photocurrent test and electrochemical impedance spectroscopy of pristine M_1Ag_{24} NCs were also conducted, and the order of charge transfer and separation efficiency of isolated NCs is the same as that of NCs-FePPc composites (Figure S24), which is in good agreement with the sequence of photocatalytic CO_2RR activity, reflecting the precisely regulation in charge transfer and photocatalytic activity by M_1Ag_{24} NCs. The lowest photoluminescence (PL) emission intensity and longest average fluorescence lifetime of Pt_1Ag_{24}-FePPc demonstrate the existence of effective charge transportation channels and the inhibition of photoinduced e^--h^+ recombination (Figure 5c, d, Table S7).

Furthermore, Mott–Schottky plot was conducted to compare the carrier density of these samples. The carrier density can be obtained by the following equation:

$$N_D = \frac{2}{e\varepsilon\varepsilon_0}\left(\frac{dC^{-2}}{dV}\right)^{-1} \quad (1)$$

where e is the elemental charge (1.6×10^{-19} C), ε_0 is the permittivity of vacuum (8.85×10^{-14} F/m), ε is the dielectric constant of the sample. For FePPc and M_1Ag_{24}-FePPc (only 3 % M_1Ag_{24} content), the dielectric constant can be regarded as the same. Therefore, the comparison of carrier density of these samples can be obtained by comparing the slopes. It can be seen from the formula that the carrier density is inversely proportional to the slope. As shown in Figure S25, the order of carrier density is Pt_1Ag_{24}-FePPc > Au_1Ag_{24}-FePPc > Ag_{25}-FePPc > FePPc, indicating Pt_1Ag_{24}-FePPc facilitates charge separation, and the tendency is in good agreement with the photocatalytic CO_2RR performance.

The Brunauer–Emmett–Teller (BET) specific surface area of M_1Ag_{24} is similar and relatively small (Ag_{25}: 2.05 m^2/g, Au_1Ag_{24}: 2.28 m^2/g, Pt_1Ag_{24}: 2.39 m^2/g), and lower than that of FePPc (6.81 m^2/g) (Figure S26a and S27a). M_1Ag_{24}-FePPc shows a similar and medium BET specific surface area (Ag_{25}-FePPc: 6.71 m^2/g, Au_1Ag_{24}-FePPc: 6.00 m^2/g, Pt_1Ag_{24}-FePPc: 5.52 m^2/g), which is due to the cluster occupation (Figure S27a). Considering that the first and most important step of CO_2RR is the adsorption and activation of CO_2, CO_2 adsorption ability was evaluated by CO_2 adsorption isotherms. The pristine M_1Ag_{24} show similar CO_2 adsorption capacities, which are all relatively small (Ag_{25}: 6.99 m^2/g, Au_1Ag_{24}: 7.74 m^2/g, Pt_1Ag_{24}: 9.50 m^2/g) (Figure S26b). In the M_1Ag_{24}-FePPc series, Pt_1Ag_{24}-FePPc exhibits the largest CO_2 adsorption capacity (Ag_{25}-FePPc:

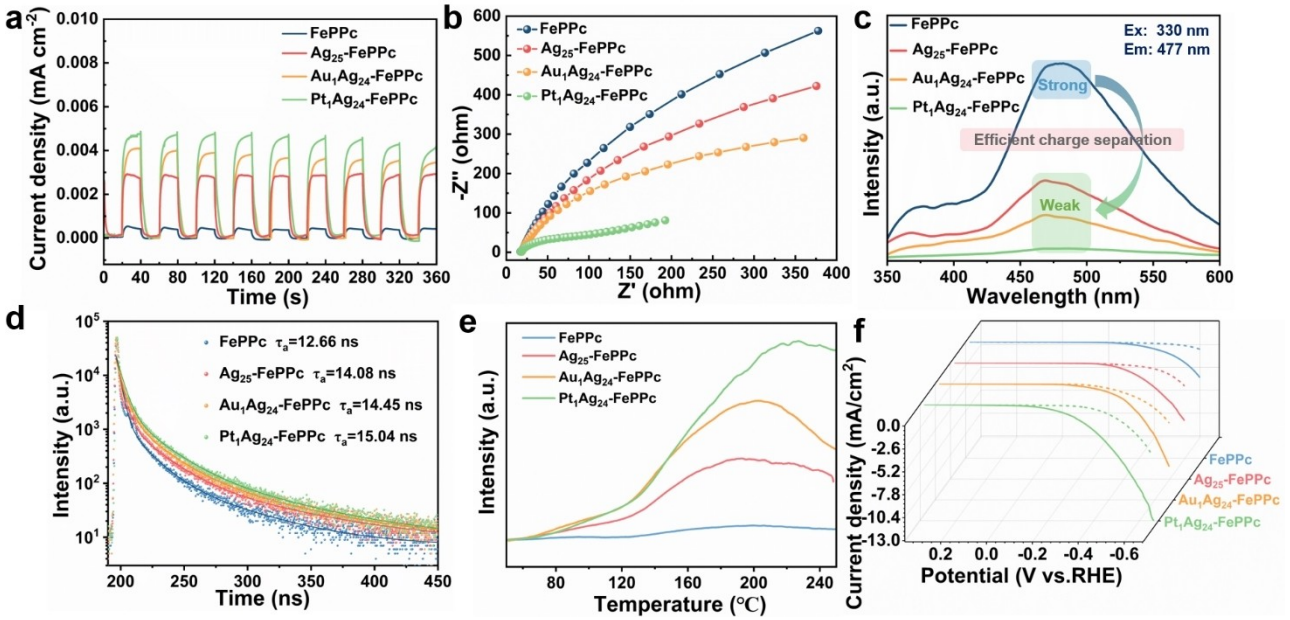

Figure 5. (a) Photocurrent responses, (b) Electrochemical impedance spectroscopy (EIS) plots, (c) PL emission spectra, (d) Time-resolved PL decay curves, (e) CO_2-TPD measurement, and (f) LSV curves recorded in Ar-saturated (dotted line) and CO_2-saturated (solid line) 0.5 M $KHCO_3$ of FePPc, Ag_{25}-FePPc, Au_1Ag_{24}-FePPc and Pt_1Ag_{24}-FePPc.

51.14 m^2/g, Au_1Ag_{24}-FePPc: 71.88 m^2/g, Pt_1Ag_{24}-FePPc: 83.14 m^2/g), although it is slightly lower than FePPc (97.31 m^2/g), which is due to the small intrinsic specific surface area caused by the cluster occupation (Figure S27b). It is worth noting that there is an obvious difference in CO_2 adsorption of M_1Ag_{24}-FePPc rather than the similarity in BET surface area of M_1Ag_{24}-FePPc (Figure S27). The order of CO_2 adsorption capacity is Pt_1Ag_{24}-FePPc > Au_1Ag_{24}-FePPc > Ag_{25}-FePPc, which is consistent with the proposed idea that Pt_1Ag_{24} leading to the most asymmetric charge distribution of FePPc is conducive to CO_2 adsorption and activation. CO_2-temperature programmed-desorption (TPD) tests were further conducted. Among the four catalysts, Pt_1Ag_{24}-FePPc exhibits the highest desorption peak intensity and temperature, indicating the strongest CO_2 adsorption ability (Figure 5e). In addition, the linear sweep voltammetry (LSV) curves under Ar and CO_2-saturated electrolyte were measured. The increased current density and decreased onset potential obtained in CO_2 compared to those in Ar can be attributed to the CO_2RR. Pt_1Ag_{24}-FePPc displays the largest difference in LSV curves between Ar and CO_2, suggesting the most favorable for CO_2 activation (Figure 5f).

Symmetry-breaking principle is regarded as an effective strategy for CO_2 activation.[18] The relative area ratio of Fe^{2+}/Fe^{3+} in FePPc is ~0.79. After combining with NC, the Fe^{2+}/Fe^{3+} ratio of M_1Ag_{24}-FePPc is increased, and it is 0.84, 1.47, and 1.65 for Ag_{25}-FePPc, Au_1Ag_{24}-FePPc, and Pt_1Ag_{24}-FePPc, respectively (Figure 6a, Table S8). The change in the ratio of Fe^{2+}/Fe^{3+} indicates that the introduction of NC causes the asymmetric charge distribution of Fe sites in FePPc, especially Pt_1Ag_{24}, which leads to the the deepest degree of charge polarization. Density functional theory (DFT) calculations were performed to Figure out the origin of the activity of Pt_1Ag_{24}-FePPc. Asymmetric charge distribution on Fe atoms is found in M_1Ag_{24}-FePPc based on bader charge analysis (Figure 6b-d). The calculated average net charge of Fe site on FePPc is 1.168^+. When M_1Ag_{24} NC is anchored on the surface of FePPc, the net charge of Fe site nearby NCs (Fe site 1) is significantly decreased, which is 0.944^+, 0.992^+, and 0.996^+ for Pt_1Ag_{24}-FePPc, Au_1Ag_{24}-FePPc, and Ag_{25}-FePPc, respectively. The net charges of Fe sites far from NCs (Fe site 2–4) are similar to the corresponding sites without NCs (Table S9, Figure S28). The charge difference between the Fe with or without M_1Ag_{24} NC anchoring follows the order: Pt_1Ag_{24}-FePPc (0.187) > Au_1Ag_{24}-FePPc (0.160) > Ag_{25}-FePPc (0.147) > FePPc (0), indicating that Pt_1Ag_{24} intrigues the most asymmetric charge distribution of Fe site in M_1Ag_{24}-FePPc, consistent with the XPS results (Figure 6e). In addition, Pt_1Ag_{24}-FePPc shows the strongest CO_2 adsorption energy of −0.243 eV, compared with other M_1Ag_{24}-FePPc and FePPc, benefiting for the first step of catalytic reaction (Table S10). Due to the small size of the clusters, it is obvious to expect that even a minor change in the structure and composition, such as a single atom change, will have a large effect on the electronic structure of the clusters, resulting in different properties. Here, due to the different types of central metal atoms, the electronic structure of clusters is different, mainly reflected in the charge negativity of the central M: Pt (−2.5) > Au (−1.9) > Ag (−1.7), according to the neutral atomic charge analysis calculation in previous work.[19] Compared to Au_1Ag_{24} and Ag_{25}, Pt_1Ag_{24} exhibits higher electron density and is more prefer donating charge when combining with FePPc, disrupting

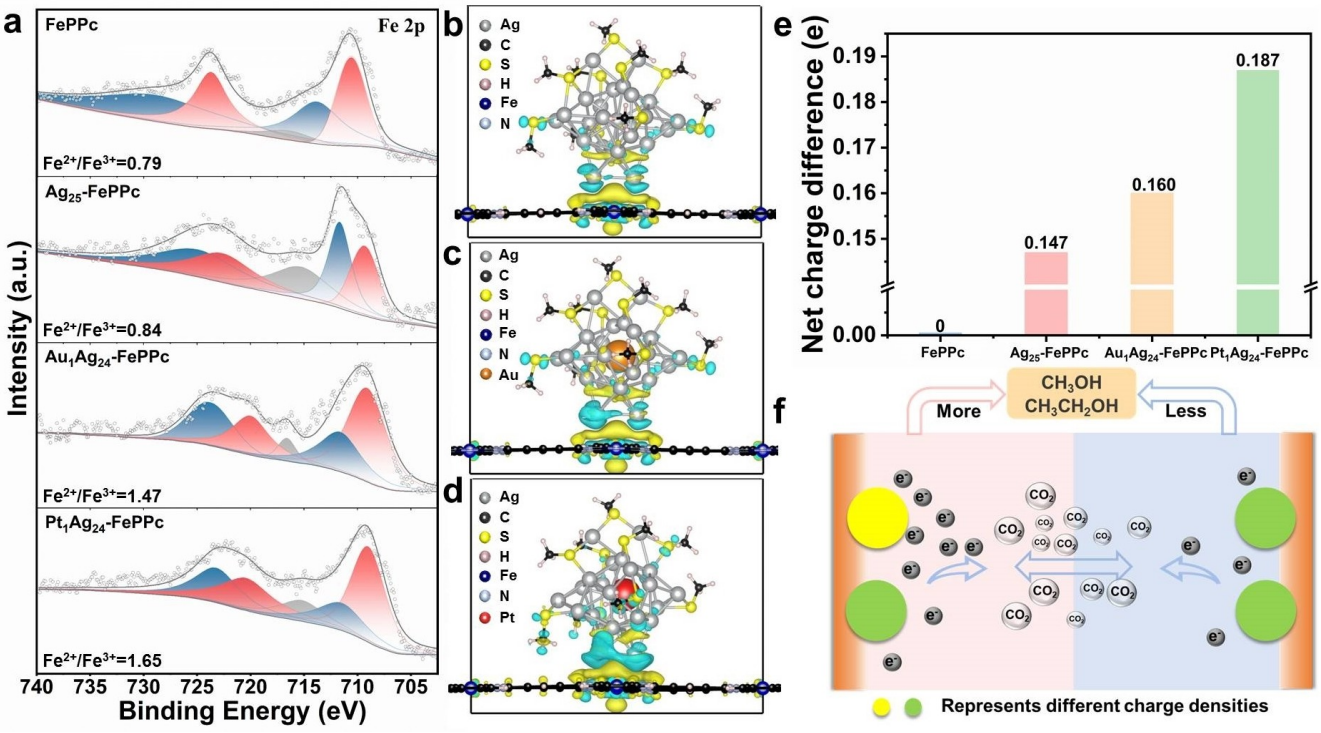

Figure 6. (a) The XPS spectra of Fe 2p for FePPc and M_1Ag_{24}-FePPc. The red and blue shaded regions correspond to the peak areas indicative of Fe^{2+} and Fe^{3+}, respectively. The differential charge density of (b) Ag_{25}-FePPc, (c) Au_1Ag_{24}-FePPc and (d) Pt_1Ag_{24}-FePPc, showing charge transfer from M_1Ag_{24} NC to FePPc. The iso-surface value is 0.0007 e^- $Bohr^{-3}$. The yellow and blue regions represent the electron accumulation and consumption regions, respectively. (e) The net charge difference between the Fe site with and without M_1Ag_{24} NC anchoring. (f) Designing asymmetric charge distribution sites to promote CO_2 reduction.

the charge balance of Fe site, making it the most asymmetric charge distribution. Therefore, based on the experimental and theoretical results, it can be inferred that Pt_1Ag_{24}-FePPc with asymmetric charge distribution could promote CO_2 reduction (Figure 6f).

In situ FT-IR was used to monitor the CO_2RR process. Under dark conditions, the peaks corresponded to CO_3^{2-} (1336 cm^{-1}) and HCO_3^- (1476, 1398 and 1219 cm^{-1}) are both observed on FePPc and Pt_1Ag_{24}-FePPc.[16b,20] Under the same time of CO_2 dark adsorption, Pt_1Ag_{24}-FePPc shows the stronger carbonate and bicarbonate peaks than FePPc, also reflecting that coupling with NC is beneficial to CO_2 adsorption and activation (Figure 7a). Under light irradiation, the initial intermediate CO_3^{2-} from the reaction of gaseous CO_2 and water vapor appears at 1942 cm^{-1}.[20a] Multiple new carbon intermediates are generated and gradually enhanced with the extension of illumination time.

The peaks at 1760 and 1560 cm^{-1} are corresponded to $*CO_2^-$, which is formed from CO_2 binding on the surface of catalyst with an electron.[21] The peak at 1409 cm^{-1} is contributed to *COOH, a crucial intermediate generated by $*CO_2^-$ reacting with a proton.[22] Then, *CO is formed at 2131 cm^{-1} when *COOH contacts with another proton and electron.[21b] Finally, CH_3OH is generated via step-by-step hydrogenation. In addition, *OCCOH, the key intermediate in C–C coupling reaction is clearly observed at 1234 cm^{-1} and its intensity is significantly increased with the light time (Figure 7b).[23] On the basis of the above in situ FT-IR analysis, the stepwise mechanism of

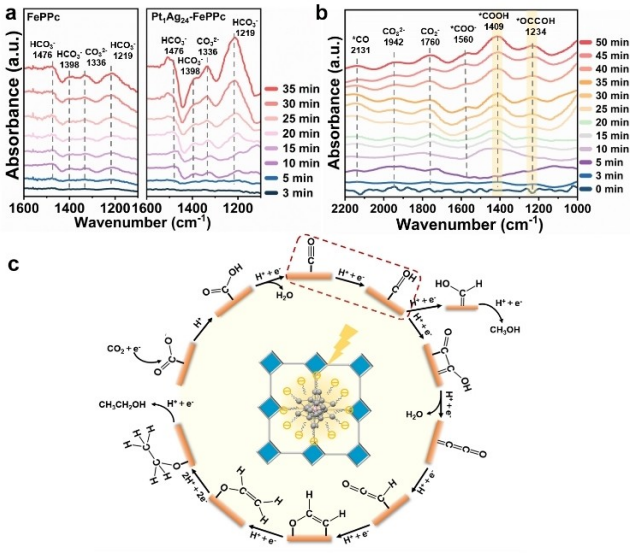

Figure 7. (a) In situ FT-IR spectra of CO_2 adsorption and activation of FePPc and Pt_1Ag_{24}-FePPc under dark conditions. (b) In situ FT-IR spectra obtained at different irradiation times during CO_2 photoreduction on Pt_1Ag_{24}-FePPc. (c) Proposed mechanism for the photoreduction of CO_2 on Pt_1Ag_{24}-FePPc.

photocatalytic CO_2RR on Pt_1Ag_{24}-FePPc is schematically proposed in Figure 7c.

Conclusions

In summary, to enhance CO_2 activation and conversion, we constructed asymmetric charge distributed sites by combining FePPc with single atom central doped Ag-based series NCs through electrostatic attraction strategy. The charge distribution of Fe sites in FePPc can be precisely regulated by heteroatom doping type in NCs. Pt_1Ag_{24} leads to the most asymmetric charge distribution of Fe sites, followed by Au_1Ag_{24} and Ag_{25}, confirmed from XPS and Bader charge analyses. Therefore, Pt_1Ag_{24}-FePPc shows the best CO_2 adsorption and activation ability, also it exhibits the most effective photoinduced charge transfer and separation. Under the conditions of visible light and pure water system, Pt_1Ag_{24}-FePPc selectively photocatalytic CO_2RR to alcohol fuels with the methanol/ethanol yield of 48.55/32.97 $\mu mol \cdot g_{cat}^{-1} \cdot h^{-1}$, higher than the counterparts. This work demonstrates the precisely regulation of asymmetric charge distribution by well-defined NCs for highly efficient CO_2 conversion.

Acknowledgements

We acknowledge the financial support of the Natural Science research project of Universities in Anhui Province (KJ2021ZD0001), Natural Science Foundation of Anhui Province (2208085MB20), Natural Science Foundation of China (52273234, 52003265). The Supercomputing Center of USTC and Hefei Advanced Computing Center are acknowledged.

Conflict of Interest

The authors declare no conflict of interest.

Data Availability Statement

The data that support the findings of this study are available in the supplementary material of this article.

Keywords: Cluster compounds · Photocatalysis · Asymmetric charge distribution · Single-atom central doping · CO_2 activation

[1] a) M. Bonchio, J. Bonin, O. Ishitani, T.-B. Lu, T. Morikawa, A. J. Morris, E. Reisner, D. Sarkar, F. M. Toma, M. Robert, *Nat. Catal.* **2023**, *6*, 657–665; b) S. Fang, M. Rahaman, J. Bharti, E. Reisner, M. Robert, G. A. Ozin, Y. H. Hu, *Rev. Methods Primers* **2023**, *3*, 61; c) B. Tang, F.-X. Xiao, *ACS Catal.* **2022**, *12*, 9023–9057.

[2] a) X. Wang, J. Jiang, L. Yang, Q. An, Q. Xu, Y. Yang, H. Guo, *Appl. Catal. B* **2024**, *340*, 123177; b) S. Bai, W. Jing, G. He, C. Liao, F. Wang, Y. Liu, L. Guo, *ACS Nano* **2023**, *17*, 10976–10986; c) J.-P. Dong, Y. Xu, X.-G. Zhang, H. Zhang, L. Yao, R. Wang, S.-Q. Zang, *Angew. Chem. Int. Ed.* **2023**, *62*, e202313648.

[3] a) K. Das, R. Das, M. Riyaz, A. Parui, D. Bagchi, A. K. Singh, A. K. Singh, C. P. Vinod, S. C. Peter, *Adv. Mater.* **2023**, *35*, 2205994; b) R. Wang, M. Zhang, S. Zhang, J. Zheng, Y. Zeng, Y. Yang, J. Ding, X. Wu, Q. Zhong, *ACS Nano* **2023**, *17*, 24363–24373.

[4] a) F. Costantino, P. V. Kamat, *ACS Energy Lett.* **2022**, *7*, 242–246; b) N.-Y. Huang, H. He, S. Liu, H.-L. Zhu, Y.-J. Li, J. Xu, J.-R. Huang, X. Wang, P.-Q. Liao, X.-M. Chen, *J. Am. Chem. Soc.* **2021**, *143*, 17424–17430.

[5] a) G. Liu, Y. Zhu, H. Gao, S. Xu, Z. Wen, L. Sun, F. Li, *ACS Catal.* **2023**, *13*, 8445–8454; b) G. Li, Z. Lian, Z. Wan, Z. Liu, J. Qian, Y. Deng, S. Zhang, Q. Zhong, *Appl. Catal. B* **2022**, *317*, 121787.

[6] T. Shi, H. Li, L. Ding, F. You, L. Ge, Q. Liu, K. Wang, *ACS Sustainable Chem. Eng.* **2019**, *7*, 3319–3328.

[7] R. Hao, J. Chen, Z. Wang, J. Zhang, Q. Gan, Y. Wang, Y. Li, W. Luo, Z. Wang, H. Yuan, C. Yan, W. Zheng, Y. Huang, P. Liu, J. Yan, K. Liu, C. Liu, Z. Lu, *Sci. China Mater.* **2021**, *64*, 2987–2996.

[8] a) S. Zhu, X. Li, X. Jiao, W. Shao, L. Li, X. Zu, J. Hu, J. Zhu, W. Yan, C. Wang, Y. Sun, Y. Xie, *Nano Lett.* **2021**, *21*, 2324–2331; b) J. Zhu, W. Shao, X. Li, X. Jiao, J. Zhu, Y. Sun, Y. Xie, *J. Am. Chem. Soc.* **2021**, *143*, 18233–18241; c) H. Liu, Y. Chen, H. Li, G. Wan, Y. Feng, W. Wang, C. Xiao, G. Zhang, Y. Xie, *Angew. Chem. Int. Ed.* **2023**, *62*, e202304562.

[9] a) X. Yan, X.-Y. Fu, F.-X. Xiao, *Adv. Funct. Mater.* **2023**, *33*, 2303737; b) M. S. Bootharaju, C. W. Lee, G. Deng, H. Kim, K. Lee, S. Lee, H. Chang, S. Lee, Y.-E. Sung, J. S. Yoo, N. Zheng, T. Hyeon, *Adv. Mater.* **2023**, *35*, 2207765.

[10] a) Y.-D. Cao, D. Yin, S. Li, X.-Y. Dong, Y. Feng, H. Liu, L.-L. Fan, G.-G. Gao, S.-Q. Zang, *Angew. Chem. Int. Ed.* **2023**, *62*, e202307678; b) H. Liang, B.-J. Liu, B. Tang, S.-C. Zhu, S. Li, X.-Z. Ge, J.-L. Li, J.-R. Zhu, F.-X. Xiao, *ACS Catal.* **2022**, *12*, 4216–4226; c) H. Wang, X. Zhang, W. Zhang, M. Zhou, H.-L. Jiang, *Angew. Chem. Int. Ed.* **2024**, e202401443.

[11] X. Kang, S. Chen, S. Jin, Y. Song, Y. Xu, H. Yu, H. Sheng, M. Zhu, *ChemElectroChem* **2016**, *3*, 1261–1265.

[12] Q. Qi, J. Hu, S. Guo, H. Song, S. Wang, Y. Yao, T. Le, W. Li, C. Zhang, L. Zhang, *Appl. Catal. B* **2021**, *299*, 120637.

[13] Z. Zhang, M. Dou, H. Liu, L. Dai, F. Wang, *Small* **2016**, *12*, 4193–4199.

[14] S. Roy, E. Reisner, *Angew. Chem. Int. Ed.* **2019**, *58*, 12180.

[15] a) W. Wan, C. A. Triana, J. Lan, J. Li, C. S. Allen, Y. Zhao, M. Iannuzzi, G. R. Patzke, *ACS Nano* **2020**, *14*, 13279–13293; b) S. Yang, Y. Yu, M. Dou, Z. Zhang, L. Dai, F. Wang, *Angew. Chem. Int. Ed.* **2019**, *58*, 14724–14730; c) S. Zhang, J. Wu, M. Zheng, X. Jin, Z. Shen, Z. Li, Y. Wang, Q. Wang, X. Wang, H. Wei, J. Zhang, P. Wang, S. Zhang, L. Yu, L. Dong, Q. Zhu, H. Zhang, J. Lu, *Nat. Commun.* **2023**, *14*, 3634.

[16] a) S. Gong, B. Ni, X. He, J. Wang, K. Jiang, D. Wu, Y. Min, H. Li, Z. Chen, *Energy Environ. Sci.* **2023**, *16*, 5956–5969; b) X. Zhao, Y. Fan, W. Zhang, X. Zhang, D. Han, L. Niu, A. Ivaska, *ACS Catal.* **2020**, *10*, 6367–6376; c) X. Han, B. Lu, X. Huang, C. Liu, S. Chen, J. Chen, Z. Zeng, S. Deng, J. Wang, *Appl. Catal. B* **2022**, *316*, 121587.

[17] Y. Nosaka, A. Y. Nosaka, *Chem. Rev.* **2017**, *117*, 11302–11336.

[18] a) H. Li, J. Zhao, L. Luo, J. Du, J. Zeng, *Acc. Chem. Res.* **2021**, *54*, 1454–1464; b) Y. Wu, Q. Hu, Q. Chen, X. Jiao, Y. Xie, *Acc. Chem. Res.* **2023**, *56*, 2500–2513.

[19] Y. Liu, X. Chai, X. Cai, M. Chen, R. Jin, W. Ding, Y. Zhu, *Angew. Chem. Int. Ed.* **2018**, *57*, 9775.
[20] a) L. Shen, Z. Xie, L. Hou, J. Yang, Q. Li, *Energy Fuels* **2022**, *36*, 11515–11523; b) R. Tang, X. a. Dong, J. Sheng, S. Xi, L. Zhang, F. Dong, *Appl. Catal. B* **2022**, *316*, 121661; c) H. Shi, H. Wang, Y. Zhou, J. Li, P. Zhai, X. Li, G. G. Gurzadyan, J. Hou, H. Yang, X. Guo, *Angew. Chem. Int. Ed.* **2022**, *61*, e202208904.
[21] a) Y. Liu, D. Shen, Q. Zhang, Y. Lin, F. Peng, *Appl. Catal. B* **2021**, *283*, 119630; b) X. Cao, D. Tan, B. Wulan, K. S. Hui, K. N. Hui, J. Zhang, *Small Methods* **2021**, *5*, 2100700.
[22] X. Yang, X. Lan, Y. Zhang, H. Li, G. Bai, *Appl. Catal. B* **2023**, *325*, 122393.
[23] K. Das, R. Das, M. Riyaz, A. Parui, D. Bagchi, A. K. Singh, A. K. Singh, C. P. Vinod, S. C. Peter, *Adv. Mater.* **2023**, *35*, 2205994.

Manuscript received: July 10, 2024
Accepted manuscript online: July 24, 2024
Version of record online: September 12, 2024